CrossMark

Effects of partial slip on entropy generation and MHD combined convection in a lid-driven porous enclosure saturated with a Cu–water nanofluid

A. J. Chamkha[1,2] · A. M. Rashad[3] · T. Armaghani[4] · M. A. Mansour[5]

Abstract

In this work, the influences of heat generation/absorption and nanofluid volume fraction on the entropy generation and MHD combined convection heat transfer in a porous enclosure filled with a Cu–water nanofluid are studied numerically with of partial slip effect. The finite volume technique is utilized to solve the dimensionless equations governing the problem. A comparison with already published studies is conducted, and the data are found to be in an excellent agreement. The minimization of entropy generation and the local heat transfer according to various values of the controlling parameters are reported in detail. The outcome indicates that an augmentation in the heat generation/absorption parameter decreases the Nusselt number. Also, when the volume fraction is raised, the Nusselt number and entropy generation are reduced. The impact of Hartmann number on heat transfer and the Richardson number on the entropy generation and the thermal rendering criteria are also presented and discussed.

Keywords Heat generation/absorption · Entropy generation · Nanofluid · Partial slip · Nusselt number

List of symbols

B	Dimensionless of heat source/sink length
B_0	Magnetic field strength (T)
Be	Bejan number
b	Length of heat source (m)
C_p	Specific heat at constant pressure (J kg K^{-1})
D	Dimensionless heat source position
Da	Darcy number
d	Location of heat sink and source (m)
H	Length of cavity (m)
Ha	Hartmann number, $B_0 L \sqrt{\sigma_f / \rho_f v_f}$
Gr	Grashof number, $g\beta_f H^3 \Delta T / v_f^2$
g	Acceleration due to gravity (m s^{-2})
K	Permeability of porous medium (m^2)
k	Thermal conductivity (W m^{-1} K^{-1})
Nu	Local Nusselt number
Nu_m	Average Nusselt number of heat source
p	Fluid pressure (Pa)
P	Dimensionless pressure, $pH/\rho_{nf}\alpha_f^2$
Pr	Prandtl number, v_f/α_f
Re	Reynolds number, $V_0 H/v_f$
S	Entropy generation (W K^{-1} m^{-3})
T	Temperature (K)
T_c	Cold wall temperature (K)
T_h	Heated wall temperature (K)
u, v	Velocity components in x, y directions (m s^{-1})
U, V	Dimensionless velocity components, u/V_0, v/V_0
x, y	Cartesian coordinates (m)
X, Y	Dimensionless coordinates, x/L, y/L

Greek symbols

α	Thermal diffusivity, m^2 s^{-1}, $k/\rho c_p$
β	Thermal expansion coefficient, K^{-1}

✉ T. Armaghani
armaghani.taher@yahoo.com

1 Mechanical Engineering Department, Prince Sultan Endowment for Energy and Environment Prince Mohammad Bin Fahd University, Al-Khobar 31952, Kingdom of Saudi Arabia

2 Rak Research and Innovation Center, American University of Ras Al Khaimah, Ras Al Khaimah, United Arab Emirates

3 Department of Mathematics, Faculty of Science, Aswan University, Aswân 81528, Egypt

4 Department of Engineering, Mahdishahr Branch, Islamic Azad University, Mahdishahr, Iran

5 Department of Mathematics, Faculty of Science, Assuit University, Assuit, Egypt

ϕ Solid volume fraction
σ Effective electrical conductivity (μS cm^{-1})
θ Dimensionless temperature, $(T - T_c)/(T_h - T_c)$
μ Dynamic viscosity (N s m^{-2})
v Kinematic viscosity (m^2 s^{-1})
ρ Density (kg m^{-3})

Subscripts
c   Cold
0   Reference
f   Pure fluid
h   Hot
m   Average
nf   Nanofluid
p   Nanoparticle

Introduction

Combined convection in enclosures saturated porous media is presented in several transport operations in engineering devices. Indeed, the combined convection is advised for altitude heat-dissipating electronic ingredients, where free convection is notable for providing effective cooling. Significance of the combined convection flow can be located in heat exchangers, solar energy storage, greasing technology, cooling the electronic systems and desiccation technologies [1–4]. Among these applications, convection in porous media with inner energy provenances is practical in the notion of thermal inflammation and in investigations considering the chemical reactions and these interested for detaching fluids [5, 6]. Also, the new suspension called nanofluid [7] can be applied to develop thermal conduct system in several engineering implementations like transport, micromechanics, instrument and cooling equipment.

A comparatively little issue of studies dealing with mixed convective of nanofluids saturated in porous medium was reported. Ahmed and Pop [8] investigated the combined convective of nanofluid over a vertical plate applying three various nanoparticles followed the common pattern of Tiwari and Das [9], which combines only the nanofluid volume fraction. Cimpean and Pop [10] considered the fully developed mixed convection flow of a nanofluid in a permeable channel. Gorla et al. [11] examined the mixed convective flow of a nanofluid adjacent to a vertical wedge embedded in porous media. Ghalambaz and Noghrehabadi [12] investigated the influences of heat generation/absorption on natural convective of nanofluids along a plate saturated porous media. Matin and Ghanbari [13] studied the Brownian motion and the thermophoresis effects on combined convection of nanofluid in a permeable channel. Recently, Srinivasacharya and Kumar [14] investigated combined convection through a wavy surface

saturated with a nanofluid in porous media. MHD mixed convective flow of a nanofluid adjacent to a vertical cylinder embedded in porous media was investigated by Jafarian et al. [15]. Some more pertinent investigations on the presented study can be found in the references [16–22].

All of the above-mentioned investigations are based on the first-law analysis. Lately, the second-law-based works have acquired concern for analyzing thermal systems. Entropy generation is applied like a gauging to evaluate the rendering of thermal systems. The studying of the energy employment and the entropy generation is one of the fundamental aims in styling a thermal system. Bejan [23–25] pointed to the several causes back to entropy generation in applied thermal engineering. Generation of entropy devastates ready mission of a system. Hence, it produces good engineering significance of focus on irreversibility of heat transfer and fluid friction operation. There are just extremely little works that study the second-law analysis in the existence of a nanofluid as an active fluid in porous medium. Many investigators [26–28] presented theoretical and numerical contributions on entropy generation due to flow and heat transfer of nanofluids in several geometries and flow regimes. The nanofluids flow along a permeable moving surface was studied by Sheikholeslami et al. [29]. They exhibited that an augment in the volume fraction reduced the momentum boundary-layer thickness and the rate of entropy generation, while the thermal boundary-layer thickness promoted. Ting et al. [30] examined the entropy generation of nanofluids flow in thermic non-equilibrium saturated porous medium in microchannels. The analysis of MHD entropy generation on non-Newtonian nanofluid through a radiate shrinking surface was investigated by Bhatti et al. [31]. Das et al. [32] also investigated the unsteady MHD entropy generation on nanofluid past accelerating stretching sheet. Ismael et al. [33] studied the entropy generation due to free convection in an enclosure domain. They suggested a novel gauge for assessment of the thermal rendering. Armaghani et al. [34] investigated the heat transfer and entropy generation of nanofluid in a partially porous media in an inclined cavity. Entropy and heat transfer analysis in a conduit partially filled with porous media-LTNE condition and exothermicity effects was studied by Torabi et al. [35].

The above studies guide us to be certain that the entropy generation and MHD combined convection in a porous enclosure filled with a nanofluid with heat generation/absorption and partial slip effects have not been studied yet. Hence, this work is the focus of the current article. It is considered that this investigation will contribute in developing the thermal rendering in several engineering devices.

Problem description and mathematical modeling

The problem of steady two-dimensional MHD mixed convection of a nanofluid inside a lid-driven square porous enclosure of length H is considered with internal heat generation Q and partial slip effects. The scheme of the current problem is displayed in Fig. 1a. A heat sink and an opposite heat source are located on a segment of the lower and upper walls, respectively, each with a length b. Two parts of the lower and upper walls of the enclosure are kept at T_c and T_h such that $T_h > T_c$ while the other parts are kept adiabatic. The left and right walls are isolated and move with a constant velocity V_0. A magnetic field with strength B_0 is applied on left side of the enclosure with angle Φ along the positive horizontal direction.

The nanofluid used in the analysis is supposed to be incompressible, laminar and exposed to internal heat generation at a uniform rate Q, and the base fluid (water) and the solid spherical nanoparticles (Cu) are in thermal equilibrium and also the solid matrix and nanofluid are in thermal equilibrium. The single-phase approach is used for modeling the nanofluid heat transfer. The thermophysical properties of the base fluid and the nanoparticles are found in Table 1. The Boussinesq approximation is performed for

the nanofluid properties to relate density variation to temperature variation and to pair in this way the temperature profiles to the flow profiles. Thus, the governing equations for steady mixed convection can be presented as, see [36, 37]:

$$\frac{\partial u}{\partial x} + \frac{\partial v}{\partial y} = 0, \tag{1}$$

$$u\frac{\partial u}{\partial x} + v\frac{\partial u}{\partial y} = -\frac{1}{\rho_{nf}}\frac{\partial p}{\partial x} + \upsilon_{nf}\left(\frac{\partial^2 u}{\partial x^2} + \frac{\partial^2 u}{\partial y^2}\right) - \frac{\upsilon_{nf}}{K}u$$
$$+ \frac{\sigma_n B_0^2}{\rho_{nf}}\left(v\sin\Phi\cos\Phi - u\sin^2\Phi\right), \tag{2}$$

$$u\frac{\partial v}{\partial x} + v\frac{\partial v}{\partial y} = -\frac{1}{\rho_{nf}}\frac{\partial p}{\partial y} + \upsilon_{nf}\left(\frac{\partial^2 v}{\partial x^2} + \frac{\partial^2 v}{\partial y^2}\right) - \frac{\upsilon_{nf}}{K}v$$
$$+ \frac{\sigma_{nf} B_0^2}{\rho_{nf}}\left(u\sin\Phi\cos\Phi - v\cos^2\Phi\right) \tag{3}$$
$$+ \frac{(\rho\beta)_{nf}}{\rho_{nf}}g(T - T_0),$$

$$u\frac{\partial T}{\partial x} + v\frac{\partial T}{\partial y} = \alpha_{nf}\left(\frac{\partial^2 T}{\partial x^2} + \frac{\partial^2 T}{\partial y^2}\right) + \frac{Q_0}{(\rho C_p)_{nf}}(T - T_0), \tag{4}$$

where u and v are the velocity components along the x- and y- axes, respectively, T is the fluid temperature, p is the
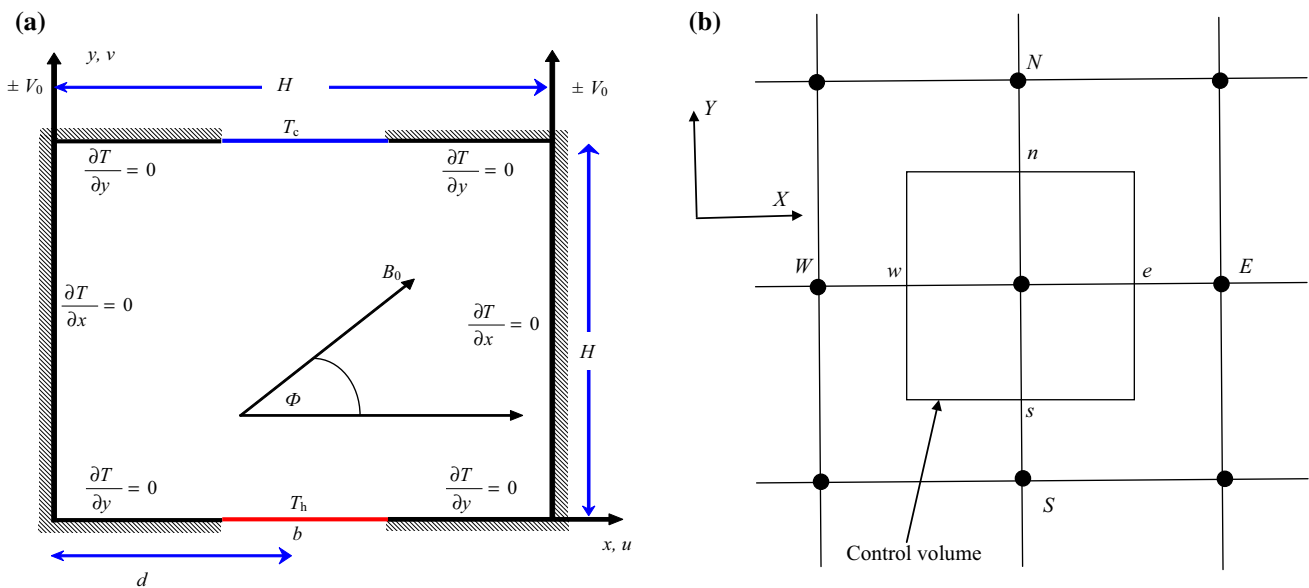

Fig. 1 a Scheme of the problem under the consideration. b Control volume for the current investigation

Table 1 Thermophysical properties of water and nanoparticle materials [42]

	$\rho/\text{kg m}^{-3}$	$C_p/\text{J kg}^{-1}\,\text{K}^{-1}$	$K^{-1}/\text{Wm}^{-1}\,\text{K}^{-1}$	β/K^{-1}
Pure water	997.1	4179	0.613	21×10^{-5}
Copper (Cu)	8933	385	401	1.67×10^{-5}

fluid pressure, g is the gravity acceleration, Q_0 is the heat generation ($Q_0 > 0$) or absorption ($Q_0 < 0$) coefficient, ρ_{nf} is the density, μ_{nf} is the dynamic viscosity, v_{nf} is the kinematic viscosity.

The boundary conditions are:

$$y = 0, \quad u = v = 0,$$

On the lower wall:
$$T = T_h, \quad (d - 0.5b) \leq x \leq (d + 0.5b),$$
$$\frac{\partial T}{\partial y} = 0 \quad \text{otherwise}$$

$$y = H, \quad u = v = 0,$$

On the top wall:
$$T = T_c, \quad (d - 0.5b) \leq x \leq (d + 0.5b),$$
$$\frac{\partial T}{\partial y} = 0 \quad \text{otherwise}$$

On the right wall:
$$x = H, \quad u = \frac{\partial T}{\partial x} = 0,$$
$$v = \lambda_r V_0 + N\mu_{nf}\frac{\partial v}{\partial x}$$

On the left wall:
$$x = 0, \quad u = \frac{\partial T}{\partial x} = 0,$$
$$v = \lambda_l V_0 + N\mu_{nf}\frac{\partial v}{\partial x}. \tag{5}$$

Thermophysical properties of nanofluid

The effective density and heat capacitance of the nanofluid are determined by [38]:

$$\rho_{nf} = (1 - \phi)\rho_f + \phi\rho_p, \tag{6}$$

$$(\rho c_p)_{nf} = (1 - \phi)(\rho c_p)_f + \phi(\rho c_p)_p. \tag{7}$$

The thermal expansion coefficient of the nanofluid can be given as Khanafer et al. [38]:

$$(\rho\beta)_{nf} = (1 - \phi)(\rho\beta)_f + \phi(\rho\beta)_p. \tag{8}$$

Thermal diffusivity, α_{nf}, of the nanofluid was introduced by Abu-Nada and Chamkha [39] as:

$$\alpha_{nf} = \frac{k_{nf}}{(\rho c_p)_{nf}}. \tag{9}$$

In Eq. (9), k_{nf} is the thermal conductivity of the nanofluid which for spherical nanoparticles, based on the Maxwell–Garnetts model [40], is:

$$\frac{k_{nf}}{k_f} = \frac{(k_p + 2k_f) - 2\phi(k_f - k_p)}{(k_p + 2k_f) + \phi(k_f - k_p)}. \tag{10}$$

The effective dynamic viscosity of the nanofluid based on the Brinkman model [41] is given by:

$$\mu_{nf} = \frac{\mu_f}{(1 - \phi)^{2.5}}. \tag{11}$$

The effective electrical conductivity of the nanofluid was presented by Maxwell [40] as

$$\frac{\sigma_{nf}}{\sigma_f} = 1 + \frac{3(\gamma - 1)\phi}{(\gamma + 2) - (\gamma - 1)\phi}, \tag{12}$$

where $\gamma = \frac{\sigma_p}{\sigma_f}$.

Dimensionless forms of equations

The following non-dimensional parameters

$$X = \frac{x}{H}, Y = \frac{y}{H}, U = \frac{u}{V_0}, V = \frac{v}{V_0},$$

$$P = \frac{p}{\rho_{nf}U^2}, \theta = \frac{(T - T_0)}{\Delta T}, Ri = \frac{Gr}{Re^2}, S_l = S_r = \frac{N\mu_f}{H},$$

$$\Delta T = (T_h - T_c), T_0 = \frac{T_c + T_h}{2},$$

$$Q = \frac{Q_0 H^2}{(\rho c_p)_f \cdot \alpha_f}, B = \frac{b}{H}, D = \frac{d}{H}, \tag{13}$$

are introduced into Eqs. (1)–(5) to yield the following dimensionless equations:

$$\frac{\partial U}{\partial X} + \frac{\partial V}{\partial Y} = 0, \tag{14}$$

$$U\frac{\partial U}{\partial X} + V\frac{\partial U}{\partial Y} = -\frac{\partial P}{\partial X} + \frac{1}{Re}\left(\frac{v_{nf}}{v_f}\right)\left(\frac{\partial^2 U}{\partial X^2} + \frac{\partial^2 U}{\partial Y^2} - \frac{U}{Da}\right)$$
$$+ \left(\frac{\rho_f}{\rho_{nf}}\right)\left(\frac{\sigma_{nf}}{\sigma_f}\right)\frac{Ha^2}{Re}(V\sin\Phi\cos\Phi - U\sin^2\Phi), \tag{15}$$

$$U\frac{\partial V}{\partial X} + V\frac{\partial V}{\partial Y} = -\frac{\partial P}{\partial Y} + \frac{1}{Re}\left(\frac{v_{nf}}{v_f}\right)\left(\frac{\partial^2 V}{\partial X^2} + \frac{\partial^2 V}{\partial Y^2} - \frac{V}{Da}\right)$$
$$+ Ri\frac{(\rho\beta)_{nf}}{\rho_{nf} \cdot \beta_f}\theta + \left(\frac{\rho_f}{\rho_{nf}}\right)\left(\frac{\sigma_{nf}}{\sigma_f}\right)\frac{Ha^2}{Re}(U\sin\Phi\cos\Phi - V\cos^2\Phi), \tag{16}$$

$$U\frac{\partial\theta}{\partial X} + V\frac{\partial\theta}{\partial Y} = \frac{1}{Pr\,Re}\frac{\alpha_{nf}}{\alpha_f}\left(\frac{\partial^2\theta}{\partial X^2} + \frac{\partial^2\theta}{\partial Y^2}\right)$$
$$+ \frac{1}{Re\,Pr}\frac{(\rho c_p)_f}{(\rho c_p)_{nf}}Q\theta, \tag{17}$$

where

$$Pr = \frac{v_f}{\alpha_f}, Re = \frac{V_0 H}{v_f}, Gr = \frac{g\beta_f H^3 \Delta T}{v_f^2},$$

$$Ha = B_0 H\sqrt{\sigma_f/\mu_f}, Da = K/H^2,$$

are the Prandtl number, Reynolds number, Grashof number, Hartmann number and Darcy number, respectively.

The dimensionless boundary conditions for Eqs. (14)–(17) are written as:

On the bottom wall:
$$Y = 0, \quad U = V = 0,$$
$$\theta = 0.5, \quad (D - 0.5B) \leq X \leq (D + 0.5B),$$
$$\frac{\partial \theta}{\partial Y} = 0 \quad \text{otherwise}$$

On the top wall:
$$Y = 1, \quad U = V = 0,$$
$$\theta = -0.5, \quad (D - 0.5B) \leq X \leq (D + 0.5B),$$
$$\frac{\partial \theta}{\partial Y} = 0 \quad \text{otherwise}$$

On the right wall:
$$X = 1 \quad U = \frac{\partial \theta}{\partial X} = 0,$$
$$V = \lambda_r + \frac{S_r}{(1 - \phi)^{2.5}} \frac{\partial V}{\partial X}$$

On the left wall:
$$X = 1, \quad U = \frac{\partial \theta}{\partial X} = 0,$$
$$V = \lambda_l + \frac{S_l}{(1 - \phi)^{2.5}} \frac{\partial V}{\partial X}.$$

$$(18)$$

The local Nusselt number is defined as:

$$Nu_s = -\frac{k_{nf}}{k_f} \left(\frac{\partial \theta}{\partial Y} \right)_{Y=0,1}, \tag{19}$$

and the average Nusselt number is defined as:

$$Nu_{m0} = \left(\frac{1}{B} \int_{D-0.5B}^{D+0.5B} Nu_s dX \right)_{Y=0},$$

$$Nu_{m1} = \left(\frac{1}{B} \int_{D-0.5B}^{D+0.5B} Nu_s dX \right)_{Y=1},$$

$$Nu_m = \frac{Nu_{m0} + Nu_{m1}}{2}. \tag{21}$$

Governing equation for entropy generation

The entropy generation in the flow profiles is caused by the non-equilibrium flow imposed by boundary conditions. According to [42, 44], the dimensional local entropy generation can be expressed by:

$$s = \left(\frac{k_{nf}}{T_0^2} \right) \left[\left(\frac{\partial T}{\partial x} \right)^2 + \left(\frac{\partial T}{\partial y} \right)^2 \right]$$
$$+ \left(\frac{\mu_{nf}}{T_0} \right) \left\{ \frac{1}{K} (u^2 + v^2) + 2 \left[\left(\frac{\partial u}{\partial x} \right)^2 + \left(\frac{\partial v}{\partial y} \right)^2 \right] \right.$$
$$\left. + \left(\frac{\partial u}{\partial y} + \frac{\partial v}{\partial x} \right)^2 \right\} + \left(\frac{\sigma_{nf}}{T_0} \right) B_0^2 (u \sin \Phi - v \cos \Phi)^2.$$

$$(22)$$

Employing the dimensionless parameters given in Eq. (14), the formulation of the dimensionless entropy generation (S) can be written as:

$$S = s \cdot \frac{H^2 \cdot T_0^2}{k_f (\Delta T)^2} = \left(\frac{k_{nf}}{k_f} \right) \left[\left(\frac{\partial \theta}{\partial X} \right)^2 + \left(\frac{\partial \theta}{\partial Y} \right)^2 \right]$$
$$+ \Theta \cdot \left(\frac{\mu_{nf}}{\mu_f} \right) \cdot Re^2 \cdot Pr^2 \left\{ \frac{1}{Da} (U^2 + V^2) \right.$$
$$\left. + 2 \left[\left(\frac{\partial U}{\partial X} \right)^2 + \left(\frac{\partial V}{\partial Y} \right)^2 \right] + \left(\frac{\partial V}{\partial X} + \frac{\partial U}{\partial Y} \right)^2 \right\}$$
$$+ \Theta \cdot \left(\frac{\sigma_{nf}}{\sigma_f} \right) \cdot Ha^2 \cdot Re^2 \cdot Pr^2 \cdot (U \sin \Phi - V \cos \Phi)^2$$
$$= Sh + Sv + Sj. \tag{23}$$

here Sh, Sv and Sj are, respectively, the dimensionless local entropy generation rate due to heat transfer, fluid fraction and Joule heating. In Eq. (23), Θ is the irreversibility factor, which defines the proportion of the viscous entropy generation to the thermal entropy generation. It is expressed as:

$$\Theta = \frac{\mu_f \cdot T_0}{k_f} \left(\frac{\alpha_f}{\Delta T H} \right)^2. \tag{24}$$

The Bejan number, Be, defined as the proportion between the entropy generation due to heat transfer by the total entropy generation, is given as:

$$Be = \frac{Sh}{S}. \tag{25}$$

With a view to current the influence of nanoparticles, the magnetic field and the difference of temperature on the average Nusselt number, total entropy generation and Bejan number, the Nusselt number ratio, total entropy generation ratio and Bejan number ratio are given as follows:

$$Nu^+ = \frac{Nu_m}{(Nu_m)_{\phi=0}} \text{ and } Nu^{++} = \frac{Nu_m}{(Nu_m)_{Ha=0}}, \tag{26}$$

$$S^+ = \frac{S}{(S)_{\phi=0}} \text{ and } S^{++} = \frac{S}{(S)_{Ha=0}}. \tag{27}$$

The thermal performance criterion can be presented as [31]:

$$\varepsilon = \frac{S}{Nu}. \tag{28}$$

In this paper, we introduce the ratio of the thermal performance as:

$$\varepsilon^+ = \frac{S^+}{Nu^+}. \tag{29}$$

Numerical solution and validation

Because of the nonlinear interactions among Eqs. (14)–(17) in the current investigation, the solution for these equations with the boundary conditions (18) and 20) can be calculated computationally by using the collocated finite volume method. In order to demonstrate this solution, let us take Eq. (15) as an example. This equation can be written as:

$$
\frac{\partial U^2}{\partial X} + \frac{\partial UV}{\partial Y} = -\frac{\partial P}{\partial X} + \frac{1}{Re}\left(\frac{v_{nf}}{v_f}\right)
$$
$$
\left(\frac{\partial}{\partial X}\left(\frac{\partial U}{\partial X}\right) + \frac{\partial}{\partial Y}\left(\frac{\partial U}{\partial Y}\right) - \frac{U}{Da}\right) \qquad (30)
$$
$$
+ \left(\frac{\rho_f}{\rho_{nf}}\right)\left(\frac{\sigma_{nf}}{\sigma_f}\right)\frac{Ha^2}{Re}\left(V\sin\Phi\cos\Phi - U\sin^2\Phi\right).
$$

Integrating this equation over the control volume presented in Fig. 1b

$$
\iint_\Omega \left[\frac{\partial U^2}{\partial X} + \frac{\partial UV}{\partial Y}\right]dXdY = -\iint_\Omega \frac{\partial P}{\partial X}dXdY
$$
$$
+ \frac{1}{Re}\left(\frac{v_{nf}}{v_f}\right)\iint_\Omega \left[\left(\frac{\partial}{\partial X}\left(\frac{\partial U}{\partial X}\right) + \frac{\partial}{\partial Y}\left(\frac{\partial U}{\partial Y}\right) - \frac{U}{Da}\right)\right]dXdY
$$
$$
+ \left(\frac{\rho_f}{\rho_{nf}}\right)\left(\frac{\sigma_{nf}}{\sigma_f}\right)\frac{Ha^2}{Re}\iint_\Omega \left[V\sin\Phi\cos\Phi - U\sin^2\Phi\right]dXdY.
$$
$$(31)$$

The upwind differencing scheme and the central difference scheme are taken for the convective terms and the diffusion terms, respectively. Evaluating these integrals and re-arranging, the following algebraic equation is obtained:

$$
a_P^U U_P = \sum_i a_i^U U_i + S^U, \qquad (32)
$$

where $i = E, W, N, S$. Similar treatments are utilized for Eqs. (16) and (17). The resulting algebraic equations have been solved iteratively, through the alternate direction implicit procedure (ADI), by utilizing the SIMPLE algorithm [45]. The velocity correction has been done utilizing the Rhie and Chow interpolation. For convergence, the under-relaxation technique has been employed. The iteration is performed until the normalized residuals of the mass, momentum, temperature and entropy generation equations become less than 10^{-6}. The non-uniform grid contains of 101×101 grid nodes in the X and Y directions, respectively. The obtained data are separated of the number of the grids. The grid independency data are found at $Ha = 10$, $Da = 10^{-3}$, $Gr = Re = 10^4$, $D = 0.5$, $B = 0.5$, $Q = 1.0$, $\Phi = 45$, $\phi = 0.05$, $S_l = S_r = 1.0$, $\lambda_l = -\lambda_r = 1.0$ and displayed in Table 2. The CPU time is also appeared in Table 3 for different Richardson numbers.

Figure 2 displays a comparison between the temperature contour reported in this investigation with those of Khanafar and Chamkha [36] and Iwatsu et al. [37]. The data show an excellent endorsement between this investigation and the previously published investigations.

Results and discussion

Eclectic data results performed by streamlines, isotherms, local and global entropy generation, local and global Bejan number, and local and average Nusselt number are illustrated in this section. The thermal rendering criterion is also presented. The effects on each of the mentioned parameters are studied for various nanofluid volume fractions ($\phi = 0$–0.2), heat generation/absorption parameters ($Q = -2$–2) and Hartmann numbers (Ha = 0–100). The outcomes are gained for the following fixed parametric values: $Da = 10^{-3}$, $\Theta = 10^{-2}$, $\Phi = 45°$, $B = 0.5$, $D = 0.5$, $S_l = S_r = 1$.

Influence of Hartmann number (Ha)

Figure 3 indicates the effect of the Hartmann number on the streamlines, isotherms, local entropy generation and the Bejan number for $Ri = 1$, $\phi = 0.05$, $\lambda_l = -\lambda_r = 1$, $Q = 1$. Generally, the effects of the buoyancy together with the enjoined boundary condition make the fluid rotates clockwise with a single-cell circulation near the left wall and counterclockwise in the middle and within the right wall. The streamlines and the core shape of the cell are more symmetric when $Ha = 0$. For $Ha = 100$, the counterclockwise rotation is stronger and more expanded than the

Table 2 Grid-independency study for Cu–water nanofluid

Grid size	41×41	61×61	81×81	91×91	101×101	121×121
Nu_m	1.469836	1.448858	1.437232	1.429925	1.424576	1.424554

Table 3 CPU time for obtaining the results at different Richardson numbers and fixed values of the other parameters

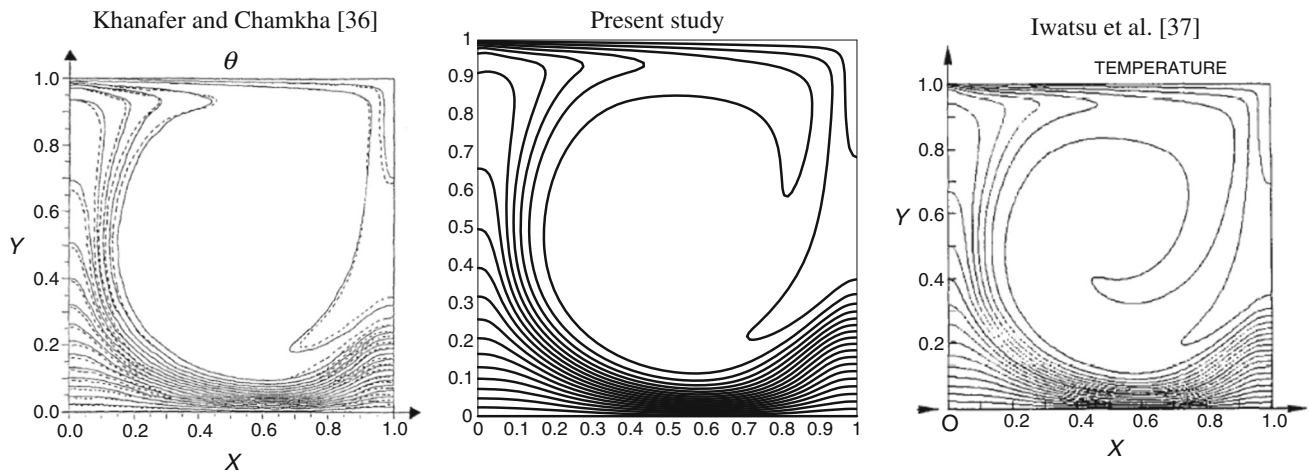|	$Ri = 0.001$	$Ri = 0.01$	$Ri = 0.1$	$Ri = 1.0$	$Ri = 10$
CPU time (min:sec)	3:35	4:38	6:26	6:46	7:09

Fig. 2 Comparison of the present study with $Re = 1000, pr = 0.71, \phi = K = 0$
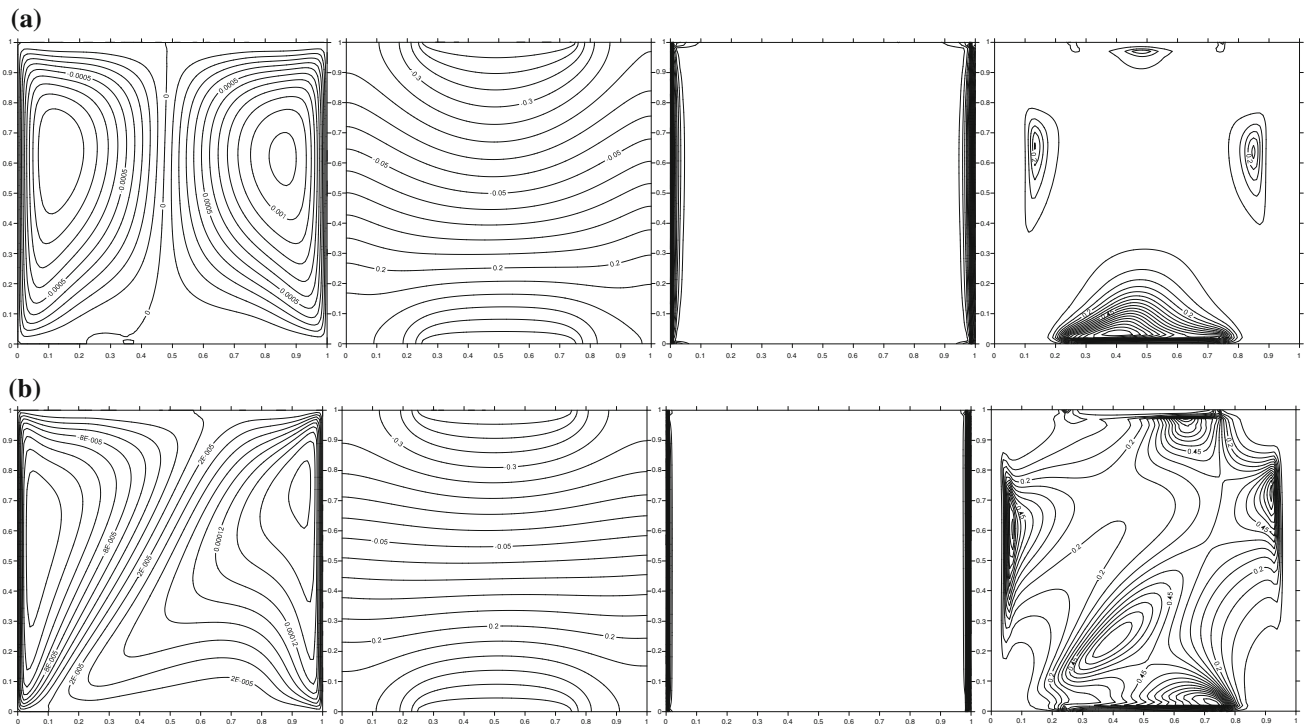

Fig. 3 Streamlines, isotherms, total entropy generation and local Bejan number, $Ri = 1, \phi = 0.05, B = 0.5, D = 0.5, \lambda_l = 1, \lambda_r = -1, Sr = S_l = 1, Q = 1$. **a** $Ha = 0$, **b** $Ha = 100$

clockwise rotation. The cells are moved to the upper of the enclosure because of the buoyancy influence and the inclined magnetic field. By enhancing the Hartmann number, the streamlines tend to be diagonal for $Ha = 100$. The isothermal lines show a similar trend for both $Ha = 0$ and $Ha = 100$. The temperature gradient near the sink and the source is greater than at other places of the cavity, and therefore, the beginning and end of the heat source and heat sink experience more heat transfer and therefore a greater

Nusselt number. The entropy generation is also significant near the left and the right walls because of the temperature gradient and the boundary layers and vanishes in the middle of the enclosure. The local Bejan number shows a more concentration at the lower and upper surfaces for $Ha = 0$ and $Ha = 100$, respectively.

As observed in Fig. 4, the local Nusselt number is decreased through raising the Hartmann number. When the Hartmann number is decreased, an augmentation in the

temperature gradient leads to enhance the Nusselt number. This reason is also being acceptable for variation in the Nusselt number with the Hartmann number within the heat source at the lower wall.

Figure 5 shows the same purpose and parameters of Fig. 3 but for $\lambda_l = \lambda_r = 1$. Contrariwise with $\lambda_l = -\lambda_r = 1$, the fluid rotates clockwise shaping a single-cell circulation. The core form of this cell is transformed from mostly vertically extended to mostly horizontally extended with two cells when Ha increases from 0 to 100. The isotherms in the center of the enclosure tend to be horizontal via increasing the Hartman number from 0 to 100. The local entropy generation is also significant within the left and right walls because the velocity and temperature gradient are sensible. The local Bejan number is significant in the center of the enclosure for $Ha = 0$, and because of the heat transfer irreversibility near the heat sink/source, the Bejan number is sizable at the upper and lower walls.

Figure 6 illustrates Nu_s for $\lambda_l = \lambda_r = 1$ at $Y = 0, 1$. As Fig. 5 indicates, for $Ha = 100$, the isothermal lines are more crowded than those corresponding to $Ha = 0$ at the beginning of the heat source, and thus, the temperature gradient has a higher value, and hence, the maximum Nusselt number happens at the beginning of the heat source for $Ha = 100$, but at the end of heat source, the temperature gradient at $Ha = 0$ is more than that for $Ha = 100$, and therefore, the Nusselt number is greater in value at $Ha = 0$ at the end of heat sink. A comparable conduct is found for the Nusselt number at $Y = 1$ in Fig. 6, but for $Ha = 0$ and $Ha = 100$, the maximum Nusselt number happens at the end and the beginning of the heat sink, respectively. Generally, at $Ha = 100$, the symmetric profiles of the isothermal lines near the heat sink and source lead to an equal value for the Nusselt number at the end and the beginning of the heat source and sink.

Influence of Richardson number (*Ri*)

The ratio of natural to forced convection modes is measured by the Richardson number. Its influence is examined by keeping the other dependent parameters at $Ha = 10, = 0.05, Q = 1$.

Figure 7 shows the influences of the Richardson number on the streamlines, isotherms, local entropy generation and the Bejan number at $\lambda_l = -\lambda_r = 1$. For $Ri = 0.001$, the predominance of forced convection can be described by the predominant shear action where two counter-rotated vortices everyone is guided by a moving wall. Moving up the core and a third vortex within the lower wall due to enhanced buoyancy effect can be observed in the streamlines for $Ri = 10$. The corresponding isotherms trend to be nearly plumed from the heat source toward the heat sink with isothermal zones localized close the moving walls and dense isotherms near the heat sink for $Ri = 0.001$. For $Ri = 10$, the isotherms tend to be horizontal in the middle of the enclosure and with approximately equal isotherms distribution on both portions of the heat sink/heat source. The formation and growth of the boundary layer and the fluid friction irreversibility lead to more generation of entropy at the top wall for $Ri = 10$ than for $Ri = 0$. The Bejan number is significant within the upper and lower walls for both of the Richardson numbers, and for $Ri = 10$ it is sensible in the middle of the cavity because of the heat transfer irreversibility.

Figure 8 indicates the influences of the Richardson number on the streamlines, isotherms, local entropy generation and the Bejan number at $\lambda_l = \lambda_r = 1$. When the
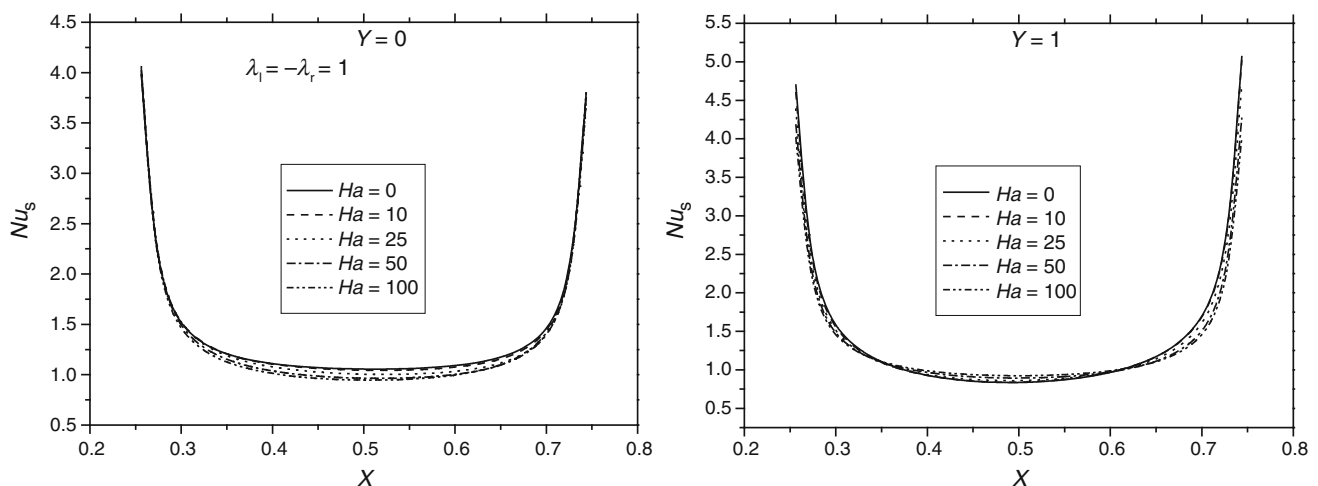

Fig. 4 Profiles for local Nusselt number for CuO–water nanofluid at $Ri = 1, \phi = 0.05, D = 0.5, B = 0.5, Sr = S_l = 1, Q = 1, \lambda_l = -\lambda_r = 1$.
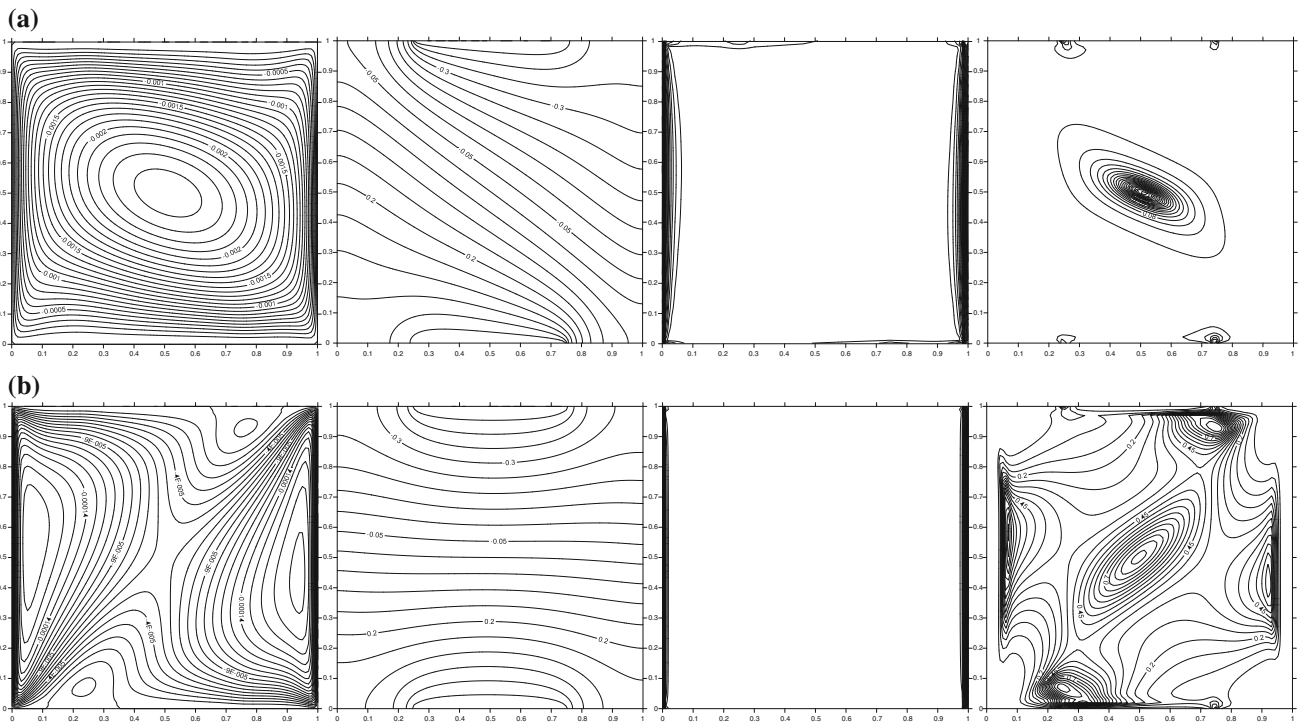
(a)

(b)

Fig. 5 Streamlines, isotherms, total entropy generation and local Bejan number $Ri = 1, \phi = 0.05, B = 0.5, D = 0.5, \lambda_l = 1, \lambda_r = 1, Sr = S_l = 1, Q = 1$. **a** $Ha = 0$, **b** $Ha = 100$
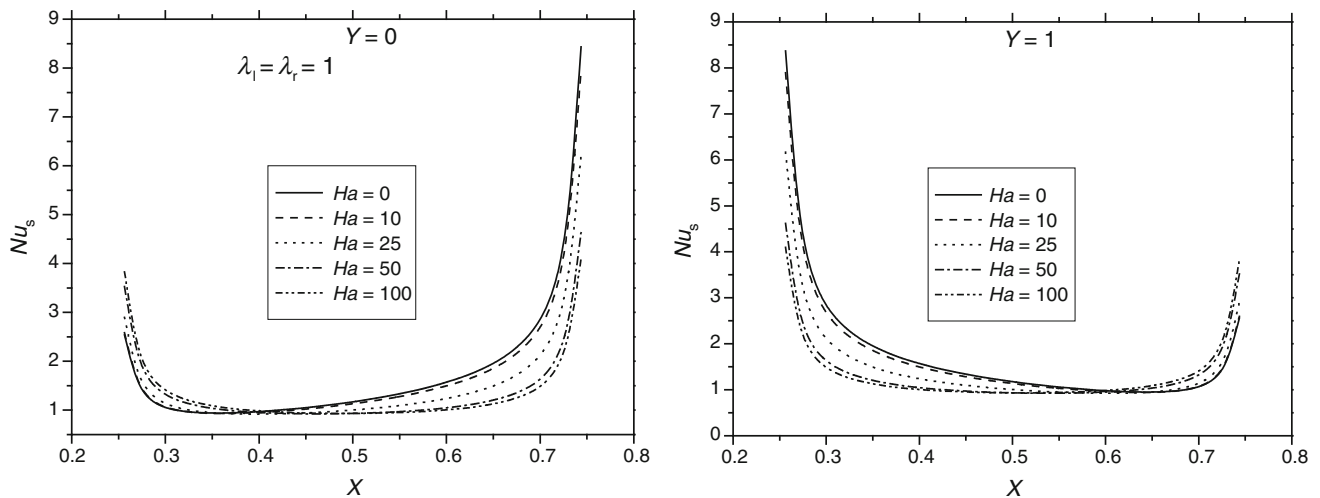

Fig. 6 Profiles of the local Nusselt number for Cu–water at $Ri = 1, \phi = 0.05, D = 0.5, B = 0.5, Sr = S_l = 1, Q = 1, \lambda_l = \lambda_r = 1$.

Richardson number is raised from 0.001 to 10 and due to the dominance of natural convection, the streamlines are strengthened and dominated by a single main clockwise circulation, while the particularly vertical isotherms disclose the ascendancy of the convection mode. By enhancing the boundary-layer thickness for $Ri = 10$ and the fluid irreversibility as well as the heat transfer

irreversibility near the walls, the entropy generation is more sensible than that for $Ri = 0.001$.

Figure 9 displays the local Nusselt number at $Y = 0, 1$ for $\lambda_l = -\lambda_r = 1 \& \lambda_l = \lambda_r = 1$. As displayed in the isotherms figures, for little Richardson number, the temperature gradient is very high within the heat sink/source, and therefore, the maximum Nusselt number happens for $Ri = 0.001$. In other words, the predominance of forced
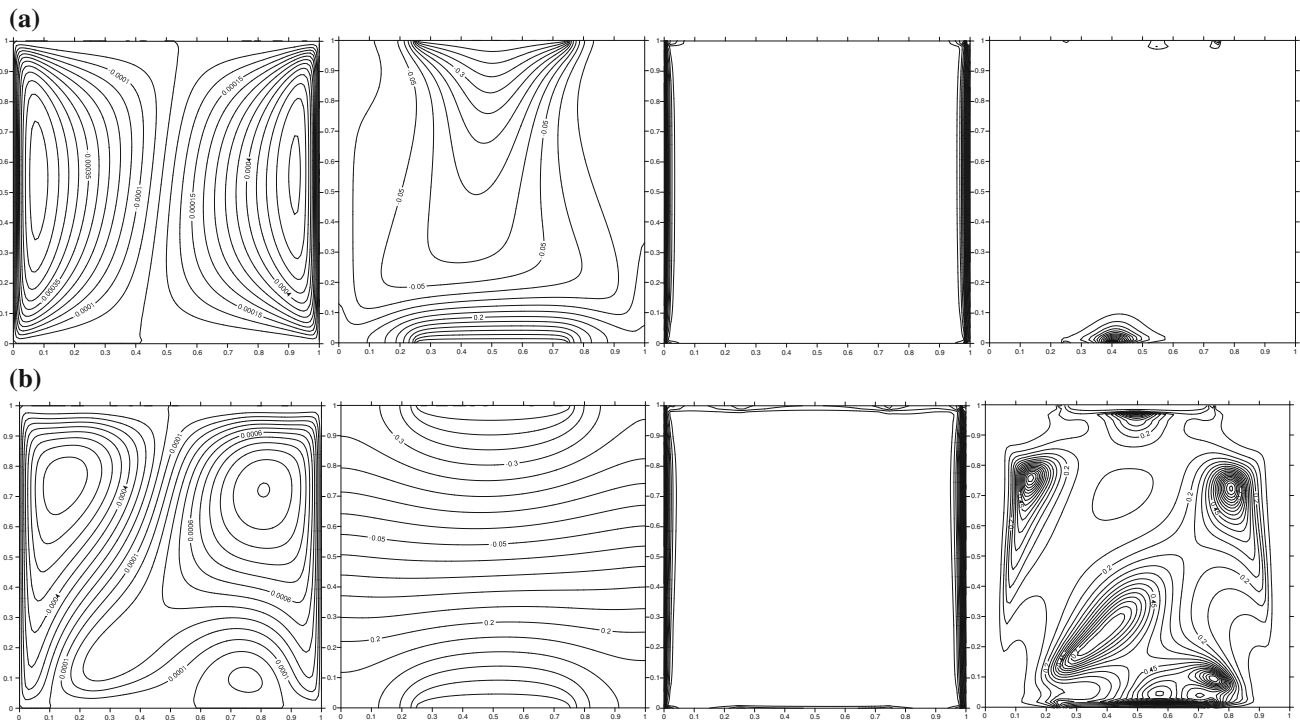
(a)

(b)

Fig. 7 Streamlines, isotherms, total entropy generation and local Bejan number $Ha = 25, \phi = 0.05, B = 0.5, D = 0.5, \lambda_l = 1, \lambda_r = -1, Sr = S_l = 1, Q = 1.$ **a** $Ri = 0.001$, **b** $Ri = 10$

convection over natural convection for low Richardson number produces an increment in heat transfer. At the beginning and the limit of the heat sink/source, the isothermal lines are very crowded, and therefore, these areas experience maximum Nusselt numbers for $Ri = 0.001$ and $\lambda_l = -\lambda_r = 1$. As displayed in Fig. 8a, the temperature gradient at the limit of the heat sink and the beginning of the heat source is very significant, and thus, the maximum Nusselt number happens at the limit of the heat source and beginning of the heat sink for Ri = 0.001 and $\lambda_l = \lambda_r = 1$.

Figure 10 displays the variation of Nu^+ with the Richardson number. Generally, by raising the nanofluid volume fraction, the average Nusselt number is decreased for all range of values of the Richardson number. Supplementing highly conductive solid nanoparticles will cause a nanofluid with an elevation in the viscosity, density and thermal conductivity. The first two properties enhance the viscous and inertia forces, respectively, while the increased thermal conductivity enhances the heat transfer. Thus, the tendency of the Nusselt number ratio is exhibited in Fig. 10. This figure elucidates that the increased viscous and inertia forces govern over the increased thermal conductivity and both the buoyancy and the shear influences as

well. This is a sensible cause for the reduction in the Nusselt number with the addition of nanoparticles. For $\varphi \leq 0.05$, the rate of reduction of Nu^+ for high Richardson numbers is more than that of low Ri values. But for $\varphi \geq 0.05$, enhancing the volume fraction shows a more reduction for Nu^+ at little Richardson numbers. The impact of enhancing the volume fraction is observed by the reduction of the entropy generation ratio (S^+) at $Ri = 1$–1000 as presented in Fig. 11. This figure indicates that S^+ is enhanced by raising the volume fraction at $Ri = 0.001$ and 0.01.

Figure 12 presents that the supplement of nanoparticles causes increment in ε^+ at low Richardson numbers ($Ri = 0.001$–1). As presented in Fig. 11a, b, ε^+ is reduced by enhancing the nanofluid volume fraction for $Ri = 100$ and 1000, and therefore, the nanoparticles addition may be useful for high Richardson numbers.

Influence of heat generation (Q)

Figures 13–16 display the influence of the heat generation parameter on the mentioned items for the constant parametric values of: $Ri = 1, Ha = 10, \lambda_l = -\lambda_r = 1$ and $\lambda_l = \lambda_r = 1$. Figures 13 and 14 display the influences of the heat
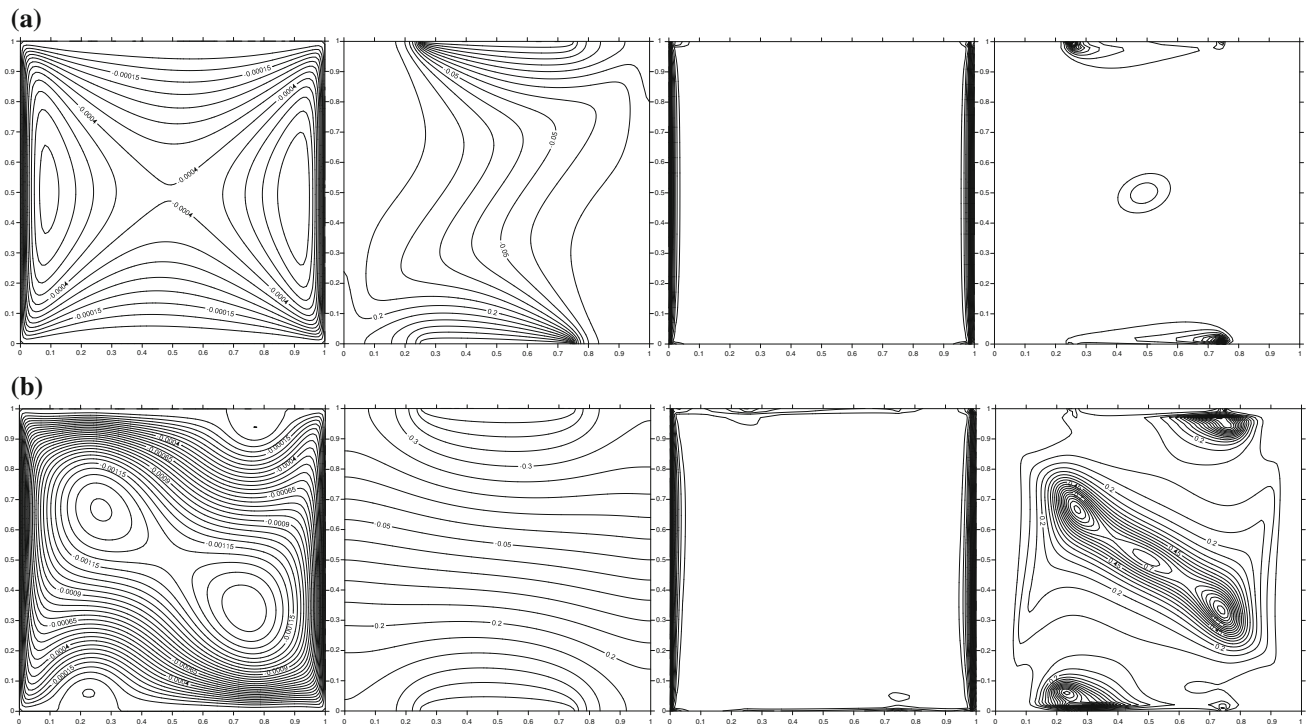
(a)

(b)

Fig. 8 Streamlines, isotherms, total entropy generation and local Bejan number $Ha = 25, \phi = 0.05, B = 0.5, D = 0.5, \lambda_l = 1, \lambda_r = 1, Sr = S_l = 1, Q = 1$. **a** $Ri = 0.001$, **b** $Ri = 10$

generation parameter on the streamlines, isotherms, entropy generation and Bejan number at $\lambda_l = -\lambda_r = 1$ and $\lambda_l = \lambda_r = 1$, respectively. The stream lines keep their general pattern with rising values of Q, but their strength and intensity are rarely decreased for both of the vertical partial slips. The isotherms in Fig. 13 exhibit that the temperature gradient is reduced within the heat source when the heat generation parameter is increased. Also, as exhibited in Fig. 14, when Q is increased, the isotherms have a tendency to be vertical in the middle of the enclosure. As displayed in Fig. 13, by raising the heat generation parameter, the local entropy generation has no significant change and the local Bejan number is vanished near the heat sink. Figure 14 also shows that the Bejan number is increased when the heat generation is enhanced.

Figure 15 shows the variation of S^+ with rising values of the volume fraction for both of $\lambda_l = -\lambda_r = 1$ and $\lambda_l = \lambda_r = 1$. It is noticed that S^+ decreases as a result of increasing φ for low nanofluid volume fractions ($\phi = 0 \cong 0.05$ for $\lambda_l = -\lambda_r = 1$ & $\varphi = 0 \cong 0.07$ for $\lambda_l = \lambda_r = 1$) and then increases with increasing φ ($\phi = 0 \geq 0.05$ for $\lambda_l = -\lambda_r = 1$ & $\varphi = 0 \geq 0.07$ for $\lambda_l = \lambda_r = 1$) for all covered ranges of

Q. It should be seen that S^+ for all ranges of values of Q and ϕ is less than unity, and therefore, adding nanoparticles to the pure fluid produces the reduction of the entropy generation. Figure 16 shows the change in ε^+ with the increment in the volume fraction. As displayed in Fig. 16, when the volume fraction is enhanced, the thermal rendering criterion is enhanced as well. The figure depicts that a little volume fraction nanofluid can be useful for this subject.

Conclusions

The influences of nanofluid volume fraction, Hartmann number, Richardson number and heat generation/absorption on the entropy generation of mixed convection in a lid-driven square porous enclosure saturated by a Cu–water nanofluid with partial slip are numerically studied. The outcomes have produced the following concluding remarks:

1. A raise in the volume fraction of the nanoparticles decreases the entropy generation inside the porous
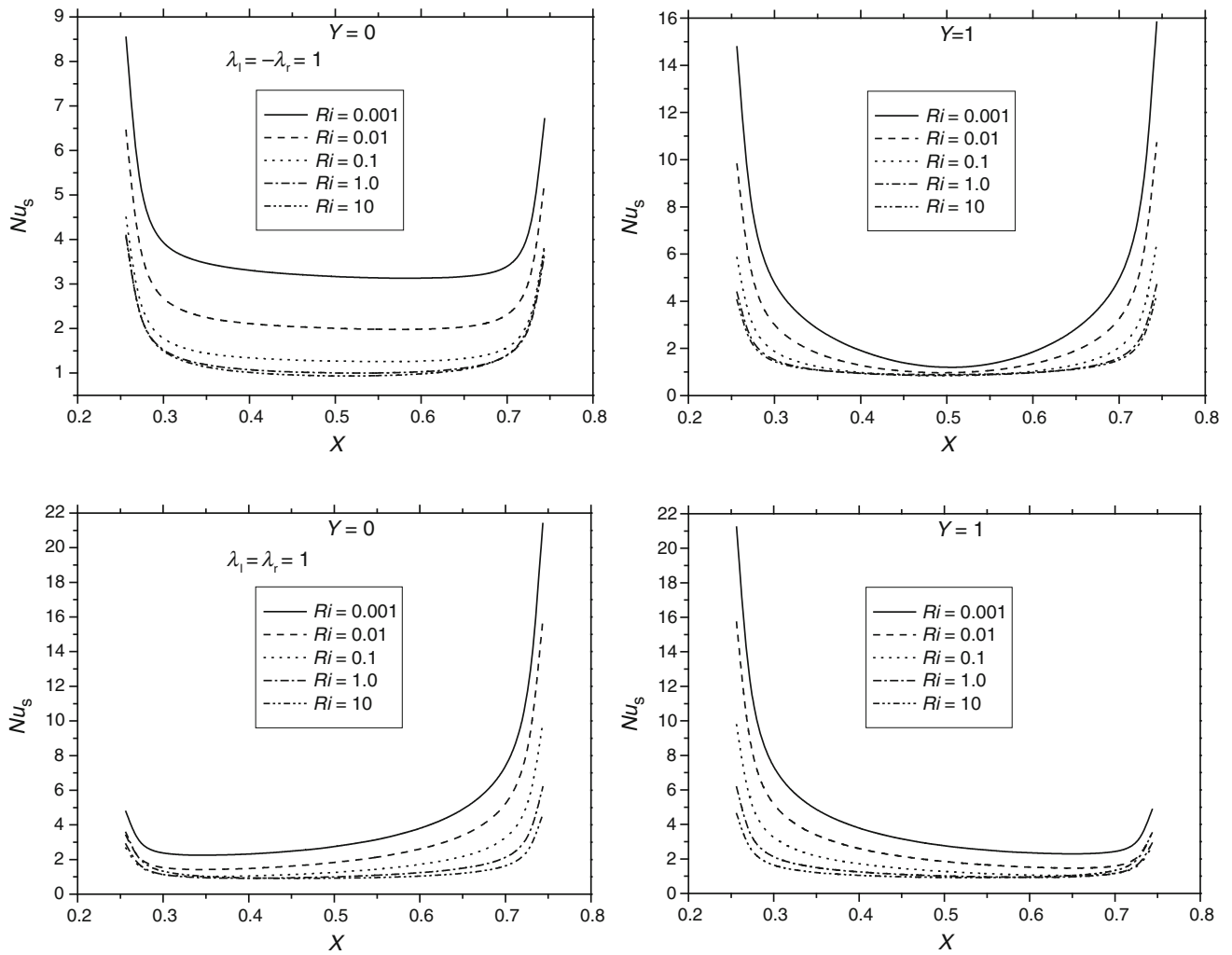
Fig. 9 Profiles of the local Nusselt number for Cu–water at $Ha = 25, \phi = 0.05, B = 0.5, D = 0.5, Sr = S_l = 1, Q = 1$
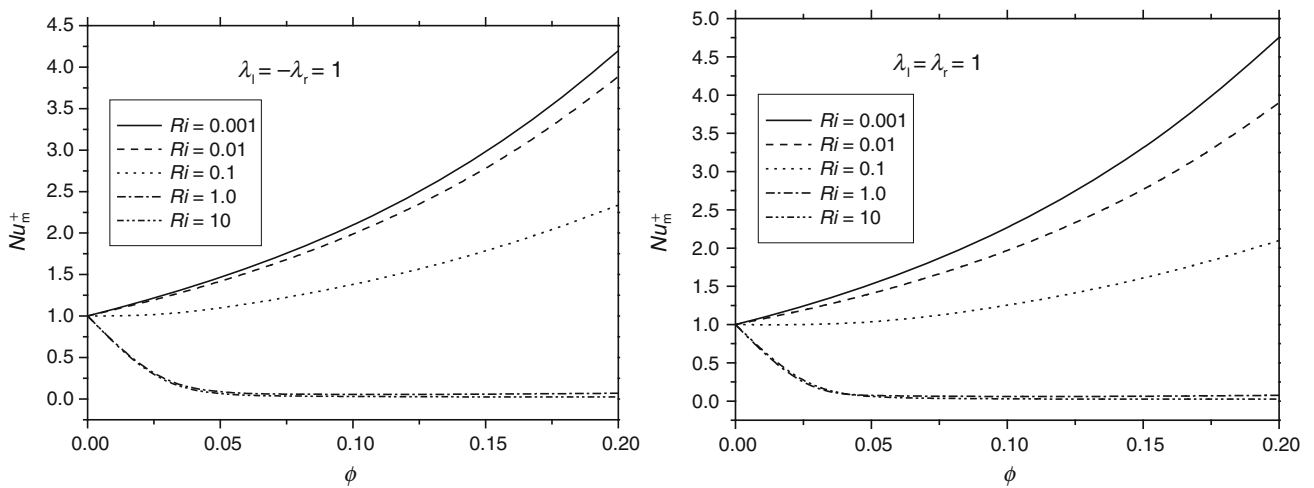

Fig. 10 Variation of the average Nusselt number ratio with Richardson number
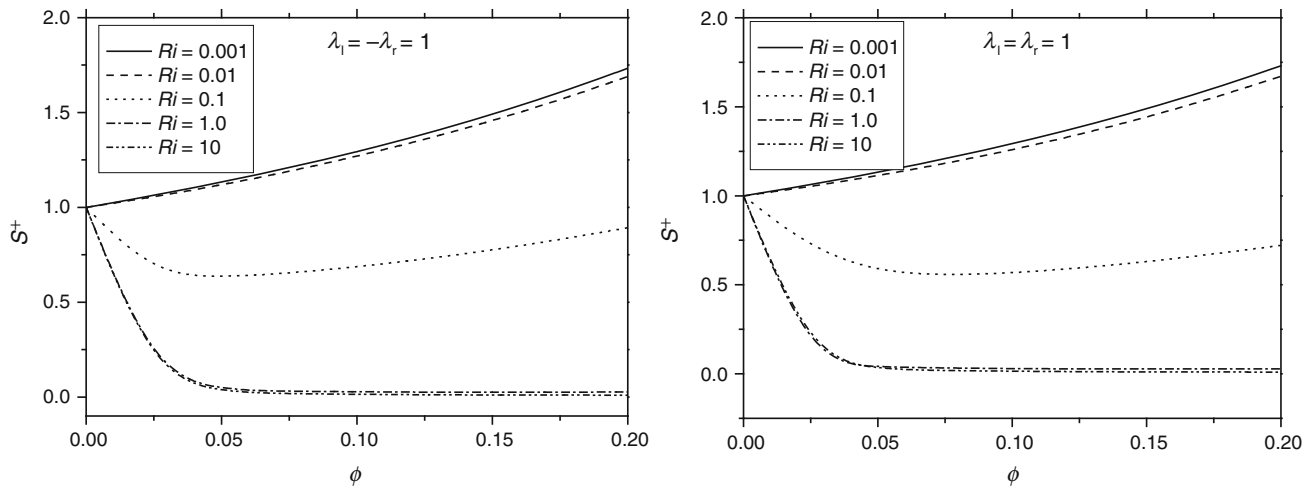
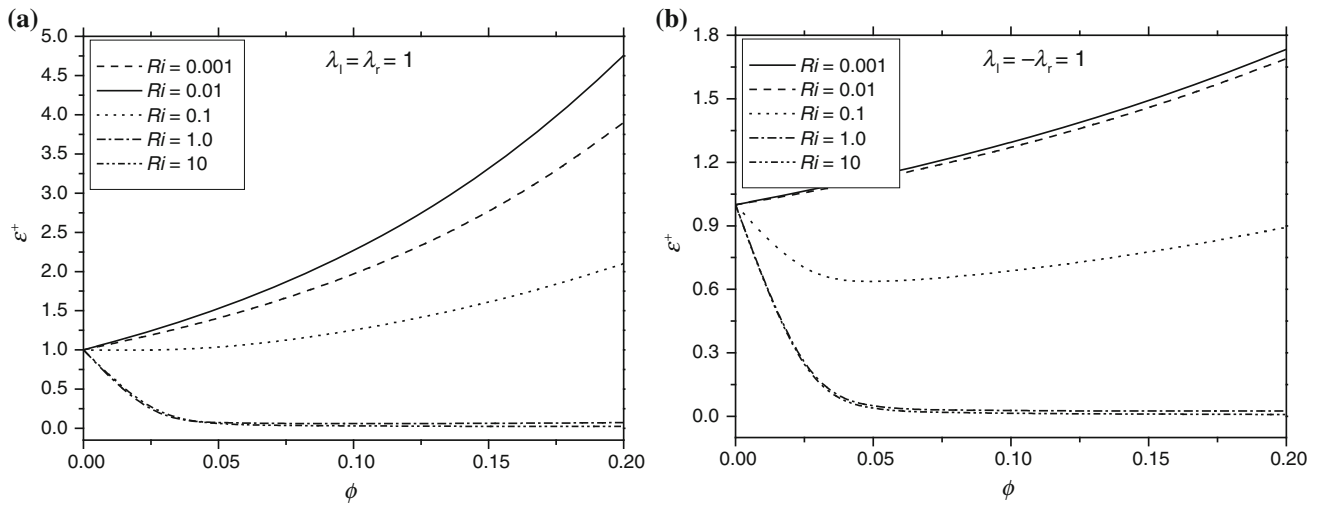**Fig. 11** Variation of the total entropy generation ratio via Richardson number

Fig. 12 Variation of $\varepsilon^+ = \frac{S^+}{Nu_m^+}$ with Richardson number. **a** $\lambda_l = 1, \lambda_r = 1$, **b** $\lambda_l = -\lambda_r = 1$

cavity for all values of the heat generation parameter Q.

2. A raise in the nanofluid volume fraction reduces the average Nusselt number for all values of the Richardson number Ri.

3. A nanofluid with small volume fraction shows a suitable effect on the thermal rendering.

4. The local Nusselt number is enhanced via raising the Hartman number.

5. The best thermal performance is seen at $Ri = 0.001$ for both $\lambda_l = -\lambda_r = 1$ and $\lambda_l = \lambda_r = 1$.

6. The Nusselt number at all ranges of the Richardson number for $\lambda_l = \lambda_r = 1$ is greater than that corresponding to $\lambda_l = -\lambda_r = 1$.
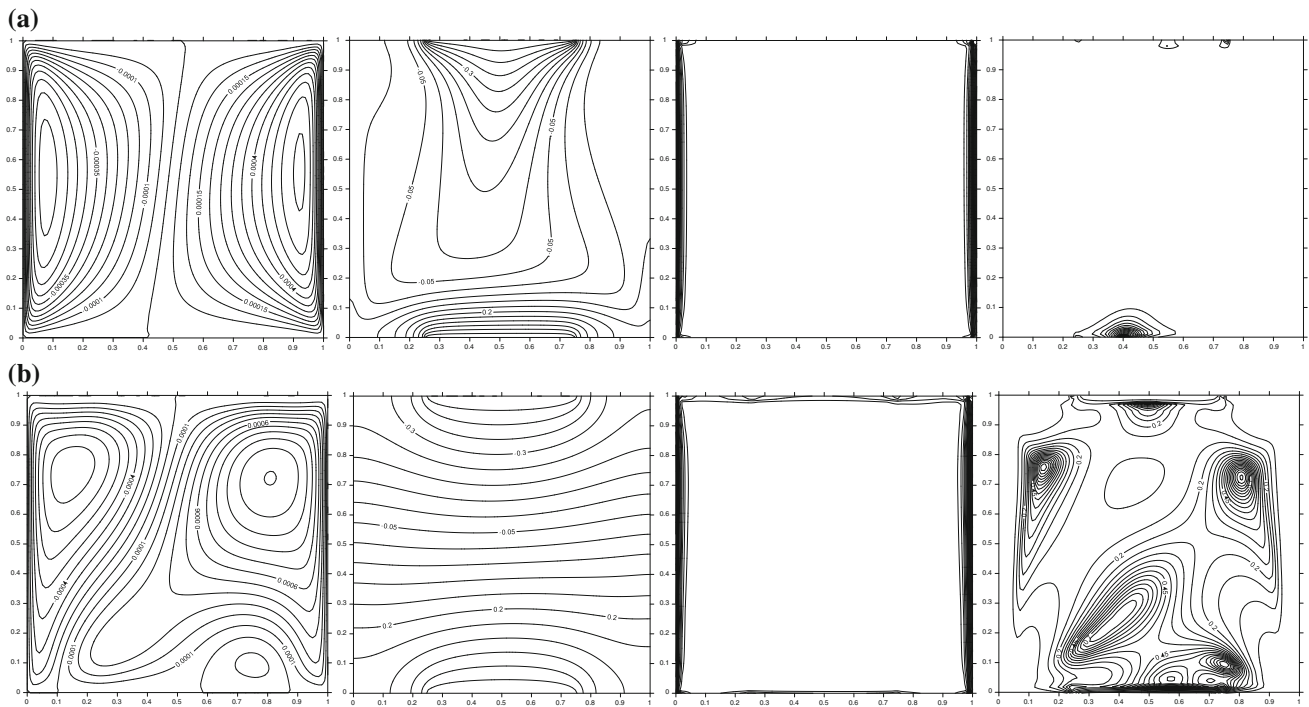
(a)

(b)

Fig. 13 Streamlines, isotherms, total entropy generation, local Bejan number at $\lambda_l = -\lambda_r = 1$. **a** $Q = -2$, **b** $Q = 2$
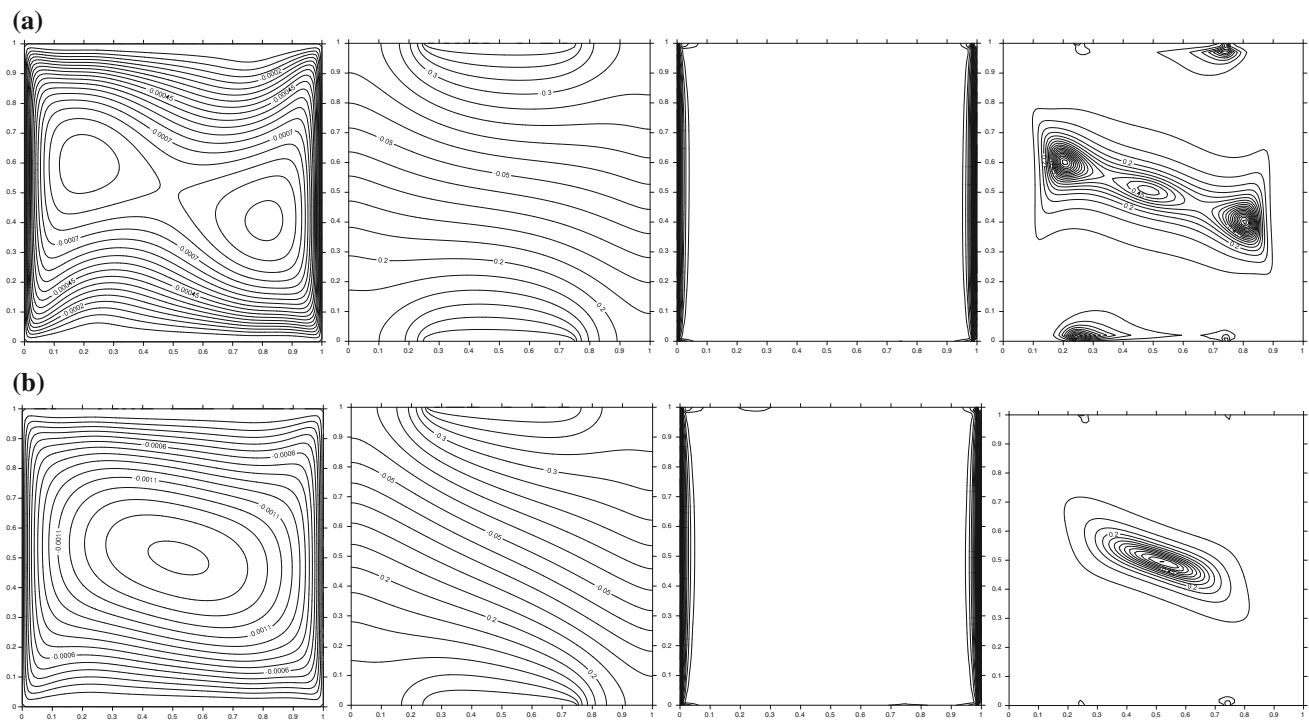
(a)

(b)

Fig. 14 Streamlines, isotherms, total entropy generation, local Bejan number at $\lambda_l = 1, \lambda_r = 1$. **a** $Q = -2$, **b** $Q = 2$
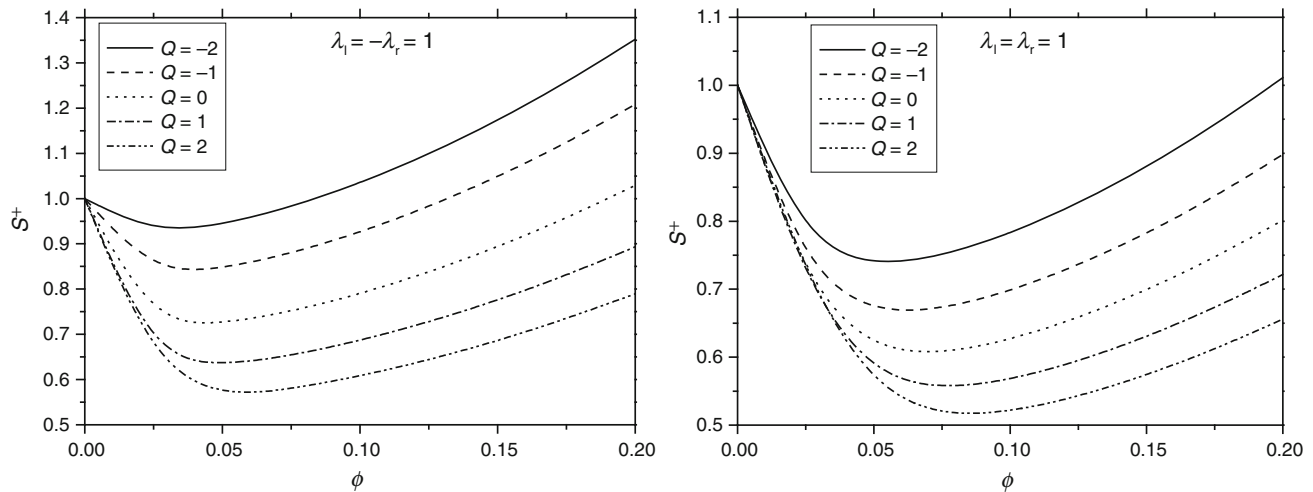
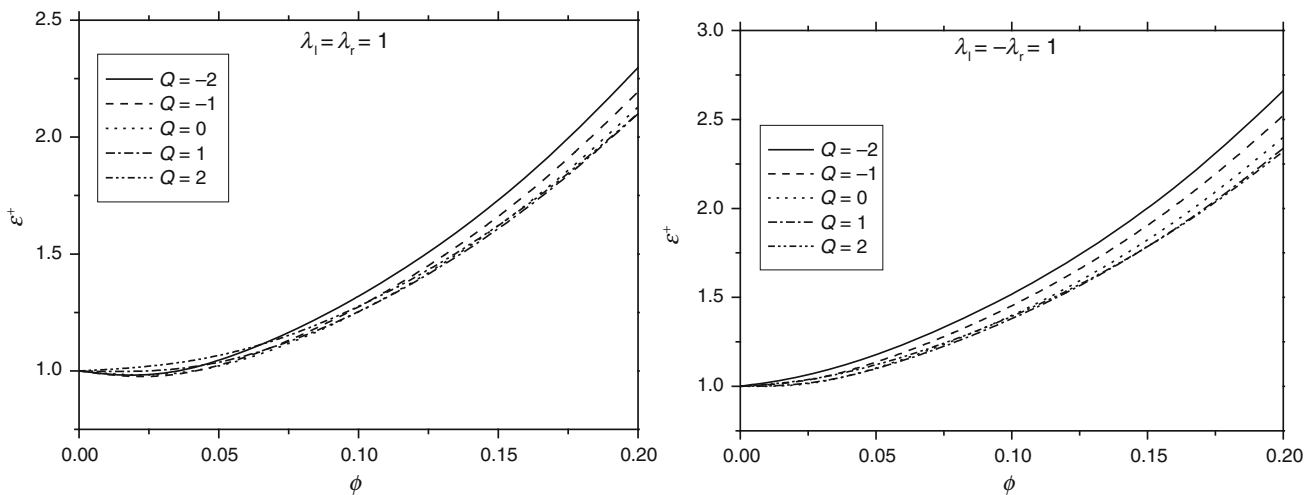**Fig. 15** Variation of the total entropy generation via heat generation

Fig. 16 Variation of ε^+ with heat generation

References

1. Khanafer KM, Al-Amiri AM, Pop I. Numerical simulation of unsteady mixed convection in a driven cavity using an externally excited sliding lid. Eur J Mech B/Fluids. 2007;26:669–87.
2. Rahman MDM, Alim MA, Saha S, Chowdhury MK. A numerical study of mixed convection in a square cavity with a heat conducting square cylinder at different locations. J Mech Eng. Instit Eng Bangl ME. 2008;39:78–85.
3. Moshizi SA, Malvandi A. Different modes of nanoparticle migration at mixed convection of Al_2O_3–water nanofluid inside a vertical microannulus in the presence of heat generation/absorption. J Therm Anal Calorim. 2016;126:1947–62.
4. Garoosi F, Rohani B, Rashidi MM. Two phase simulation of natural convection and mixed convection of the nanofluid in a square cavity with internal and external heating. Powder Technol. 2015;275:304–21.
5. Mashaei PR, Shahryari M, Madani S. Numerical hydrothermal analysis of water–Al_2O_3 nanofluid forced convection in a narrow annulus filled by porous medium considering variable properties. J Therm Anal Calorim. 2016;126:891–904.
6. Hady FM, Ibrahim FS, Abdel Gaied SM, Eid MR. Effect of heat generation/absorption natural convective boundary layer flow from a vertical cone embedded in a porous medium filled with a non-Newtonian nanofluid. Int Commun Heat Mass Transfer. 2011;38:1414–20.
7. Choi SUS. Enhancing thermal conductivity of fluid with nanoparticles. Dev Appl Non-Newtonian Flows. 1995;66:99–105.
8. Ahmad S, Pop I. Mixed convection boundary layer flow from a vertical flat plate embedded in a porous medium filled with nanofluids. Int Commun Heat Mass Transf. 2010;37(8):987–91.
9. Tiwari RK, Das MK. Heat transfer augmentation in a two-sided lid-driven differentially heated square cavity utilizing nanofluids. Int J Heat Mass Transf. 2007;50:2002–18.
10. Cimpean DS, Pop I. Fully developed mixed convection flow of a nanofluid through an inclined channel filled with a porous medium. Int J Heat Mass Transf. 2012;55:907–14.
11. Gorla RSR, Chamkha AJ, Rashad AM. Mixed convective boundary layer flow over a vertical wedge embedded in a porous medium saturated with a nanofluid-natural convection dominated regime. Nanoscale Res Lett. 2011;6:207–14.
12. Ghalambaz M, Noghrehabadi A. Effects of heat generation/absorption on natural convection of nanofluids over the vertical

plate embedded in a porous medium using drift flux model. J Comput Appl Res Mech Eng. 2014;3:113–24.

13. Matin MH, Ghanbari B. Effects of Brownian motion and thermophoresis on the mixed convection of nanofluid in a porous channel including flow reversal. Transp Porous Media. 2014;101:115–36.

14. Srinivasacharya D, Kumar PV. Mixed convection along an inclined wavy surface in a nanofluid saturated porous medium with wall heat flux. J Nanofluids. 2016;5:120–9.

15. Jafarian B, Hajipour M, Khademi R. Conjugate heat transfer of MHD non-Darcy mixed convection flow of a nanofluid over a vertical slender hollow cylinder embedded in porous media. Transp Phenom Nano and Micro Scales. 2016;4:1–10.

16. Esfe MH, Akbari M, Karimipour A, Afrand M, Mahian O, Wongwises S. Mixed-convection flow and heat transfer in an inclined cavity equipped to a hot obstacle using nanofluids considering temperature-dependent properties. Int J Heat Mass Transf. 2015;85:656–66.

17. Rashidi I, Mahian O, Lorenzini G, Biserni C, Wongwises S. Natural convection of Al_2O_3/water nanofluid in a square cavity: effects of heterogeneous heating. Int J Heat Mass Transf. 2014;74:391–402.

18. Heris SZ, Pour MB, Mahian O, Wongwises S. A comparative experimental study on the natural convection heat transfer of different metal oxide nanopowders suspended in turbine oil inside an inclined cavity. Int J Heat Mass Transf. 2014;73:231–8.

19. Ho CJ, Chen D, Yan W, Mahian O. Buoyancy-driven flow of nanofluids in a cavity considering the Ludwig-Soret effect and sedimentation: numerical study and experimental validation. Int J Heat Mass Transf. 2014;77:684–94.

20. Estellé P, Mahia O, Maré T, Öztop HF. Natural convection of CNT water-based nanofluids in a differentially heated square cavity. J Therm Anal Calorim. 2017;128:1765–70.

21. Mahian O, Kianifar A, Heris SZ, Wongwises S. Natural convection of silica nanofluids in square and triangular enclosures: theoretical and experimental study. Int J Heat Mass Transf. 2016;99:792–804.

22. Kasaeian A, Azarian RD, Mahian O, Kolsi L, Chamkha AJ, Wongwises S, Pop I. Nanofluid flow and heat transfer in porous media: a review of the latest developments. Int J Heat Mass Transf. 2017;107:778–91.

23. Bejan A. A study of entropy generation in fundamental convective heat transfer. J Heat Transf. 1979;101:718–25.

24. Bejan A. Second-law analysis in heat and thermal design. Adv Heat Transf. 1982;15:1–58.

25. Bejan A. Entropy generation minimization. Boca Raton: CRC Press; 1996.

26. Mahian O, Kianifar A, Kleinstreuer C, Al-Nimr MA, Pop I, Sahin AZ, Wongwises S. A review of entropy generation in nanofluid flow. Int J Heat Mass Transf. 2013;65:514–32.

27. Armaghani T, Kasaeipoor A, Alavi N, Rashidi MM. Numerical investigation of water-alumina nanofluid natural convection heat transfer and entropy generation in a baffled L-shaped cavity. J Mol Liq. 2016;223:243–51.

28. Chamkha AJ, Ismael MA, Kasaeipoor A, Armaghani T. Entropy generation and natural convection of CuO–water nanofluid in C-Shaped cavity under magnetic field. Entropy. 2016;18:50–60.

29. Sheikholeslami M, Ellahi R, Ashorynejad HR, Domairry G, Hayat T. Effects of heat transfer in flow of nanofluids over a permeable stretching wall in a porous medium. J Comput Theor Nanosci. 2014;11:486–96.

30. Ting TW, Hung YM, Guo N. Entropy generation of viscous dissipative nanofluid flow in thermal non-equilibrium porous media embedded in microchannels. Int J Heat Mass Transf. 2015;81:862–77.

31. Bhatti MM, Abbas T, Rashidi MM. Numerical study of entropy generation with nonlinear thermal radiation on magnetohydrodynamics non-Newtonian nanofluid through a porous shrinking sheet. J Magnet. 2016;21:468–75.

32. Das S, Chakraborty S, Jana RN, Makinde OD. Entropy analysis of unsteady magneto-nanofluid flow past accelerating stretching sheet with convective boundary condition. Applied Mathematics and Mechanics. 36;12:1593–1610.

33. Ismael MA, Armaghani T, Chamkha AJ. Conjugate heat transfer and entropy generation in a cavity filled with a nanofluid-saturated porous media and heated by a triangular solid. J Taiwan Inst Chem Eng. 2016;59:138–51.

34. Armaghani T, Ismael MA, Chamkha AJ. Analysis of entropy generation and natural convection in an inclined partially porous layered cavity filled with a nanofluid. Canadian J of Physics. to be published.

35. Torabi M, Karimi N, Zhang K, Peterson GP. Generation of entropy and forced convection of heat in a conduit partially filled with porous media-Local thermal non-equilibrium and exothermicity effects. Appl Therm Eng. 2016;106:518–36.

36. Khanafer KM, Chamkha AJ. Mixed convection flow in a lid-driven enclosure filled with a fluid-saturated porous medium. Int J Heat Mass Transf. 1999;42:2465–81.

37. Iwatsu R, Hyun JM, Kuwahara K. Mixed convection in a driven cavity with a stable vertical temperature gradient. Int J Heat Mass Transf. 1993;36:1601–8.

38. Khanafer KM, Vafai K, Lightstone M. Buoyancy-driven heat transfer enhancement in a two dimensional enclosure utilizing nanofluids. Int J Heat Mass Transf. 2003;46:3639–53.

39. Abu-Nada E, Chamkha AJ. Effect of nanofluid variable properties on natural convection in enclosures filled with an CuO–EG–water nanofluid. Int J Thermal Sci. 2010;49:2339–52.

40. Maxwell JA. Treatise on electricity and magnetism. 2nd ed. Cambridge: Oxford University Press; 1904.

41. Brinkman HC. The viscosity of concentrated suspensions and solution. J Chem Phys. 1952;20:571–81.

42. Chamkha AJ, Ismael MA. Conjugate heat transfer in a porous cavity filled with nanofluids and heated by a triangular thick wall. Int J Therm Sci. 2013;67:135–51.

43. Mahmud S, Fraser RA. Magnetohydrodynamic free convection and entropy generation in a square porous cavity. Int J Heat Mass Transf. 2004;47:3245–56.

44. Abolbashari MH, Freidoonimehr N, Nazari F, Rashidi MM. Analytical modeling of entropy generation for Casson nano-fluid flow induced by a stretching surface. Adv Powder Technol. 2015;26:542–52.

45. Patankar SV. Numerical heat transfer and fluid flow. hemisphere, New York. 1980.